



Article

Esterification of Levulinic Acid to Methyl Levulinate over Zr-MOFs Catalysts

Daiana A. Bravo Fuchineco ¹, Angélica C. Heredia ¹, Sandra M. Mendoza ², Enrique Rodríguez-Castellón ^{3,*} and Mónica E. Crivello ¹

¹ Centro de Investigación y Tecnología Química (CITeQ), Consejo Nacional de Investigaciones Científicas y Técnicas (CONICET), Facultad Regional Córdoba, Universidad Tecnológica Nacional (UTN-FRC), Córdoba 5016, Santa Fe, Argentina; dbravo@frc.utn.edu.ar (D.A.B.F.); angelicaheredia@gmail.com (A.C.H.); mcrivello@frc.utn.edu.ar (M.E.C.)

² Consejo Nacional de Investigaciones Científicas y Técnicas (CONICET), Facultad Regional Reconquista, Universidad Tecnológica Nacional (UTN-FRRQ), Reconquista 3560, Santa Fe, Argentina; smendoza@frrq.utn.edu.ar

³ Departamento de Química Inorgánica, Cristalografía y Mineralogía, Facultad de Ciencias, Universidad de Málaga, 29071 Málaga, Spain

* Correspondence: castellon@uma.es

Abstract: At present, the trend towards partial replacement of petroleum-derived fuels by those from the revaluation of biomass has become of great importance. An effective strategy for processing complex biomass feedstocks involves prior conversion to simpler compounds (platform molecules) that are more easily transformed in subsequent reactions. This study analyzes the metal–organic frameworks (MOFs) that contain Zr metal clusters formed by ligands of terephthalic acid (UiO-66) and aminoterephthalic acid (UiO-66-NH₂), as active and stable catalysts for the esterification of levulinic acid with methanol. An alternative synthesis is presented by means of ultrasonic stirring at room temperature and 60 °C, in order to improve the structural properties of the catalysts. They were analyzed by X-ray diffraction, scanning electron microscopy, infrared spectroscopy, X-ray photoelectron spectroscopy, microwave plasma atomic emission spectroscopy, acidity measurement, and N₂ adsorption. The catalytic reaction was carried out in a batch system and under pressure in an autoclave. Its progress was followed by gas chromatography and mass spectrometry. Parameters such as temperature, catalyst mass, and molar ratio of reactants were optimized to improve the catalytic performance. The MOF that presented the highest activity and selectivity to the desired product was obtained by synthesis with ultrasound and 60 °C with aminoterephthalic acid. The methyl levulinate yield was 67.77% in batch at 5 h and 85.89% in an autoclave at 1 h. An analysis of the kinetic parameters of the reaction is presented. The spent material can be activated by ethanol washing allowing the catalytic activity to be maintained in the recycles.

Keywords: UiO-66; UiO-66-NH₂; levulinic acid; methyl levulinate; esterification kinetics; batch and pressure reactions



Citation: Bravo Fuchineco, D.A.; Heredia, A.C.; Mendoza, S.M.; Rodríguez-Castellón, E.; Crivello, M.E. Esterification of Levulinic Acid to Methyl Levulinate over Zr-MOFs Catalysts. *ChemEngineering* **2022**, *6*, 26. <https://doi.org/10.3390/chemengineering6020026>

Academic Editors: Miguel A. Vicente, Raquel Trujillano and Francisco Martín Labajos

Received: 27 January 2022

Accepted: 23 March 2022

Published: 25 March 2022

Publisher's Note: MDPI stays neutral with regard to jurisdictional claims in published maps and institutional affiliations.



Copyright: © 2022 by the authors. Licensee MDPI, Basel, Switzerland. This article is an open access article distributed under the terms and conditions of the Creative Commons Attribution (CC BY) license (<https://creativecommons.org/licenses/by/4.0/>).

1. Introduction

In recent decades, due to the finite reserves and environmental pollution problems of fossil energy, governments have put forward the “energy strategy”, stimulating the utilization of renewable energy and resources [1]. The development of new technologies for producing energy and chemicals from them has prompted biomass valorization to become an important area of research. Biomass provides an ideal alternative to fossil resources; indeed, biomass is the only sustainable source of organic compounds and has been proposed as the ideal equivalent to petroleum for the production of fuels and chemicals [2]. In general, biomass is defined as all organic matter, including crops, food, plants, and

farming and forestry residues, which can be used as a source of energy [1,3]. Lignocellulose, the most abundant form of biomass, is composed of three primary components; cellulose (40–50 wt%), hemicellulose (25–30 wt%), and lignin (15–30 wt%), a phenolic polymer. Woody, herbaceous plants, and other crop residues such as sugarcane bagasse, and wheat straw, are suitable lignocellulosic feedstocks applied in the biorefinery process, to proffer valuable applications that can be derived from the petroleum-based source [2,4]. There are various available methods, through which biomass can be converted to different viable products that depend on the catalyst selected and the reaction conditions. For example, sorbitol is obtained by hydrogenation, fructose through isomerization, and 5-hydroxymethylfurfural via dehydration; this can be further transformed into levulinic acid (LA) and formic acid (FA) by hydrolysis [4,5].

Levulinic acid (LA), which is considered as one of the most promising platform molecules, has been hailed as the chemical bridge between biomass and petroleum [6,7], since it can be transformed into special chemicals such as fuels, solvents, monomers for polymers, plasticizers, surfactants, agrochemicals, and pharmaceuticals [8–10]. Within these levulinate esters are unique potential value-added energy chemicals that have significantly attracted remarkable attention of global researchers. Possessing great commercial importance due to their applications as fuel-blending components, bio-lubricants, refining of mineral oils, chemicals synthesis/synthetic reagent, polymer precursor, foam comprising material, resin precursors, green solvents, plasticizer, food flavor agent, coating composition, pharmaceutical/cosmetics, degreasing surface agent/stain removal, and building blocks for polycarbonate and herbicides synthesis [11,12].

In particular, levulinate esters have specific properties which make them suitable additives for fuels; some of them are low toxicity, high lubricity, flash point stability, and moderate flow under low-temperature conditions. [13]. Levulinic esters can be prepared by acid-catalyzed alcoholysis and are usually synthesized using homogeneous acid catalysts such as H_2SO_4 , HCl , and H_3PO_4 [9,14,15]; however, these liquid acids involved in homogeneous industrial catalytic processes generally suffer from high toxicity and corrosivity, high cost of regeneration or quenching as well as a large number of noxious byproducts and waste. A major challenge for the efficient preparation of levulinic esters is to develop robust, selective, inexpensive, and eco-friendly catalysts [6,12].

Acid solids are used as heterogeneous catalysts for the replacement of homogeneous catalysts, due to their low corrosivity, high selectivity, and easy separation from the reaction system. It is worth noting that MOFs, a new class of crystalline porous hybrid materials composed of metal ions/clusters and multi-topic organic linkers, have shown great potential as emerging porous materials due to their highly tunable textures, such as porosity, adjustable pore size, structural diversity, surface areas, and chemical functionalities [16–20].

MOF UiO-66 was synthesized for the first time in 2008 by scientists from the Universitet i Oslo (UiO) using a solvothermal treatment at 120 °C in dimethylformamide as solvent [21,22]. The MOF UiO-66-NH₂ developed by Kandiah et al., 2010, is formed of metal clusters, made up of six zirconium atoms $\text{Zr}_6\text{O}_4(\text{OH})_4$, joined together by $\mu_3\text{-O}$ and $\mu_3\text{-OH}$ groups, coming from the organic 2-aminoterephthalate ligand [23,24].

Given the Lewis acid character of UiO-66 type materials and their noticeable thermal, chemical, and mechanical stability, these materials could be good candidates for the esterification of levulinic acid using various alcohols [25–28]. In particular, it has been shown that the activity of UiO-66-NH₂ in the esterification of levulinic acid (LA) produces a reaction enhancing effect due to the close position of the NH₂ group to the metal center, allowing simultaneous activation of both LA such as alcohol. UiO-66-NH₂ behaves as a bifunctional acid–base catalyst [29,30].

The aim of this work is to evaluate the activity of organic–metal frameworks (MOFs) in fine chemistry reactions, such as the esterification of levulinic acid with methanol. For this purpose, the MOFs UiO-66 and UiO-66-NH₂ were synthesized by the solvothermal method, varying certain conditions such as their stirring method. These reactions were carried out in two systems, one batch and the other under pressure.

2. Materials and Methods

2.1. Chemicals and Reagents

Analytical grade reagents were used for the preparation of catalysts and catalytic reactions. $ZrCl_4$ ($\geq 98\%$, Merck, Darmstadt, Alemania), terephthalic acid (BDC, 98%, Aldrich, Saint Louis, MO, USA), aminoterephthalic acid (NH_2 -BDC, 98%, Aldrich, Saint Louis, MO, USA), N,N -dimetilformamide (DMF $\geq 99.8\%$, Biopack, Buenos Aires, Argentina), Acetone (99.5% Sintorgan, Buenos Aires, Argentina), Methanol ($\geq 99.5\%$, Biopack, Buenos Aires, Argentina), and Levulinic Ácid (98%, Aldrich, Saint Louis, MO, USA) were employed as received.

2.2. Synthesis of MOF UiO-66 and UiO-66- NH_2

MOFs UiO-66 and UiO-66- NH_2 were obtained by solvothermal method [21,31,32]. Two different binding agents of terephthalic acid (BDC) or aminoterephthalic acid (NH_2 -BDC) were used. The synthesis was carried out by magnetic and ultrasonic stirring, the latter at room temperature or 60 °C. The samples were named as M_X , M_X -U, or M_X -UT, where “X” can be “A” related to synthesis with BDC or “B” related to synthesis with NH_2 -BDC. The letter U indicates the synthesis on ultrasound at room temperature. The letters U-T indicate the synthesis on ultrasound at 60 °C of temperature.

The synthesis consisted of dissolving 1.042 g in 50 mL of $ZrCl_4$ in 50 mL of the solvent (DMF); the solution was magnetic or ultrasonic stirred for 5 min. In the case of ultrasound synthesis, the container is placed inside ultrasound equipment, which works at room temperature or at 60 °C. Then, 0.708 g of terephthalic acid or 0.788 g of aminoterephthalic acid was incorporated. The mixture was kept under stirring (magnetic or ultrasonic) for 30 min. The gel was transferred to a Teflon-lined stainless-steel autoclave and kept in an oven at 120 °C for 24 h. The material obtained was immersed in DMF and then washed with acetone with a lower boiling point and easily removed. The precipitate was separated by centrifugation. Finally, the solid was dried at 90 °C for 24 h, obtaining ~1.404 g and ~1.735 g of a white (A) or yellow (B) solid powder, respectively.

2.3. Characterization of MOF UiO-66 and UiO-66- NH_2

XRD powder patterns were collected on an X'pert diffractometer (PANanalytical, Netherlands) using monochromatized Cu $K\alpha$ radiation ($\lambda = 1.54 \text{ \AA}$) at a scan speed of $0.25^\circ \text{ min}^{-1}$ in 2θ .

Infrared analyses were carried out on a spectrophotometer Smartomi-Transmission Nicolet iS10 Thermo Scientific (Thermo Scientific, Waltham, MA, USA) in a range of $4000\text{--}400 \text{ cm}^{-1}$.

The micrographs of the mixed oxides were obtained by SEM instrument model JSM-6380 LV (JEOL, Japan) equipped with a Supra 40 (Carl Zeiss, Oberkochen, Germany), the samples were metalized with chromium.

The specific surface area (SSA), analysis was carried out in an ASAP 2020 instrument (Micromeritics, Norcross, GA, USA) and was calculated by the Brunauer–Emmett–Teller (BET) method.

X-ray photoelectron spectra (XPS) were recorded with a PHI VersaProbe II Scanning XPS Microprobe (Physical Electronics, Chanhassen, MN, USA) with scanning monochromatic X-ray Al $K\alpha$ radiation as the excitation source (100 μm area analyzed, 52.8 W, 15 kV, 1486.6 eV), and a charge neutralizer. The pressure in the analysis chamber was maintained below 2.0×10^{-6} Pa. High-resolution spectra were recorded at a given take-off angle of 45 by a multi-channel hemispherical electron analyzer operating in the constant pass energy mode at 29.35 eV. Spectra were charge referenced with the C 1s of adventitious carbon at 284.8 eV. The energy scale was calibrated using Cu $2p_{3/2}$, Ag $3d_{5/2}$, and Au $4f_{7/2}$ photoelectron lines at 932.7, 368.2, and 83.95 eV, respectively. The Multipack software version 9.6.0.15 was employed to analyze in detail the recorded spectra. The obtained spectra were fitted using Gaussian–Lorentzian curves to more accurately extract the binding energies of the different element core levels.

In order to carry out the elemental analysis, samples were acid-digested in a closed-vessel microwave oven (SCP Science, Baie-D'Urfe, QC, Canada). The chemical quantification was performed by microwave plasma atomic emission spectroscopy (MP-AES), using an Agilent 4200 MP AES instrument (Agilent, Santa Clara, CA, USA).

To study surface acidity, the adsorbed CO molecules were measured by FTIR analysis at two different temperatures (50 °C and 100 °C) in a Nicolet iS10 instrument. Initially, samples were treated under vacuum and then were put in contact with CO molecules during 2 h at room temperature.

2.4. Catalytic Esterification Reaction

The synthesized MOFs were used for the catalytic esterification of levulinic acid and methanol (Figure 1), with a 1:15 molar ratio and 0.05 g of the solid [25,33–36]. Two reaction systems were used. On the one hand, the reaction was carried out in a glass batch reactor with magnetic stirring at 65 °C, coupled to a reflux condenser. The total time was 5 h and 0.15 mL of samples were collected from the reaction medium at 0, 1, 2, 3, 4, and 5 h. The time $t = 0$ h was the time at which the temperature of the reaction medium reached 65 °C. Samples were collected using a microsyringe equipped with a filter (Whatman paper filter n° 5) to remove catalyst particles. On the other hand, a pressure system was used constituted of an autoclave reactor. The reactor was placed inside an oven at 130 °C with magnetic stirring at 400 rpm. It was previously purged with N₂ and then pressurized to 30 bar. The reaction products were analyzed by gas chromatography and mass spectrometry. It was used on an Agilent Technologies 7820A instrument equipped with a HP-20M column and a Perkin Elmer Clarus 560 instrument.

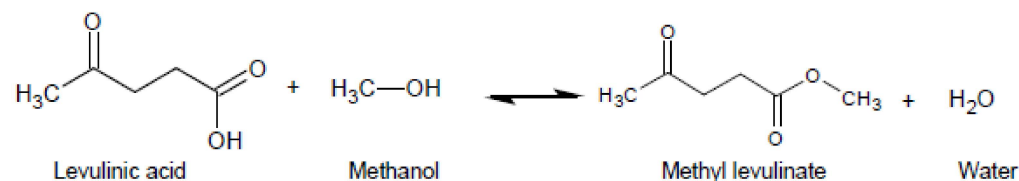


Figure 1. Esterification reaction of levulinic acid with methanol.

We calculated the LA conversion (%C), selectivity (%S), and yield (%Y) of products and identified $n_{(LA)I}$ and $n_{(LA)F}$ as the initial and final concentrations of levulinic acid, and $n_{(ML)}$ as the concentration of methyl levulinate.

$$\% C = \frac{n_{(LA)I} - n_{(LA)F}}{n_{(LA)I}} \times 100 \quad (1)$$

$$\% S = \frac{n_{(ML)}}{n_{(LA)I} - n_{(LA)F}} \times 100 \quad (2)$$

$$\% Y = \frac{C \times S}{100} \quad (3)$$

3. Results

3.1. Physicochemical Characterization

3.1.1. X-ray Diffraction

Figure 2 shows the X-ray diffraction patterns of the MOFs. Two peaks located close to 2θ of 7.4, 8.5, and 25.6° are associated with the diffraction by (1 1 1), (2 0 0), and (600) planes characteristic of the MOF UiO-66-NH₂. [22,37–39]. The M_A-U and M_A-UT samples show an exchange in the intensity of the main peaks (111) and (002) and the appearance of a new peak at 2θ angle of ~17.6° related to a phase change, is the same as that reported in the literature [22]. This behavior could be promoted by temperature and ultrasound applied in the synthesis. On the other hand, the XRD patterns in series B show peaks of similar intensity with good crystalline order, regardless of the applied treatment [40].

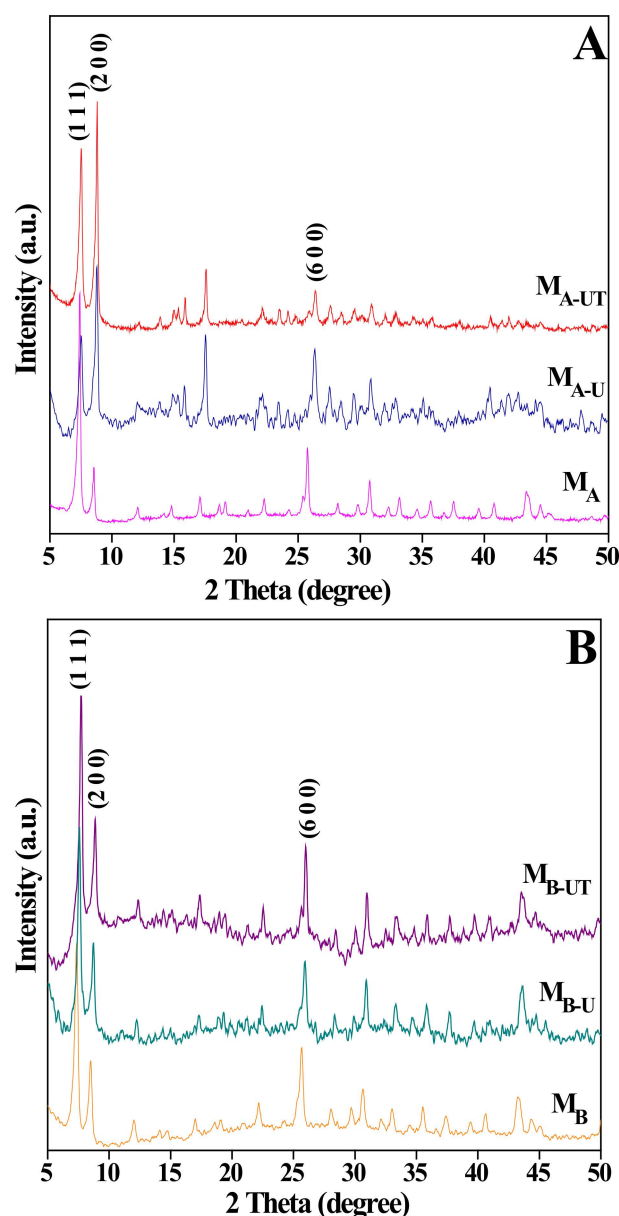


Figure 2. X-ray diffraction patterns. (A) UiO-66 magnetic stirring (M_A), UiO-66 ultrasound stirring (M_{A-U}), and ultrasound stirring at 60 °C (M_{A-UT}). (B) UiO-66 magnetic stirring (M_B), UiO-66 ultrasound stirring (M_{B-U}), and ultrasound stirring at 60 °C (M_{B-UT}).

3.1.2. FTIR Spectroscopy

The chemical states and functional groups of the different samples were investigated by FT-IR (Figure 3). The peaks at 1586 and 1395 cm^{-1} are attributed to the asymmetric and symmetric stretching vibrations of the COO^- groups in the terephthalic acid, and the peak at 1506 cm^{-1} is the typical peaks of the $\text{C}=\text{C}$ peak of the vibration of the aromatic ring. The two lowest frequencies at 488 cm^{-1} belong to the stretching vibrations of $\text{Zr}-\text{O}$ in the Zr_6 cluster, and the band at 551 cm^{-1} is assigned to the asymmetric stretching vibration of $\text{Zr}(\text{OC})$. For the case of materials with the $\text{BDC}-\text{NH}_2$ ligand, the signals at 3449 and 3348 cm^{-1} corresponded with the amine symmetric and asymmetric stretching bands, while the signals at 1258 and 1386 cm^{-1} were attributed to $\text{C}-\text{N}$ binding absorption [41–43].

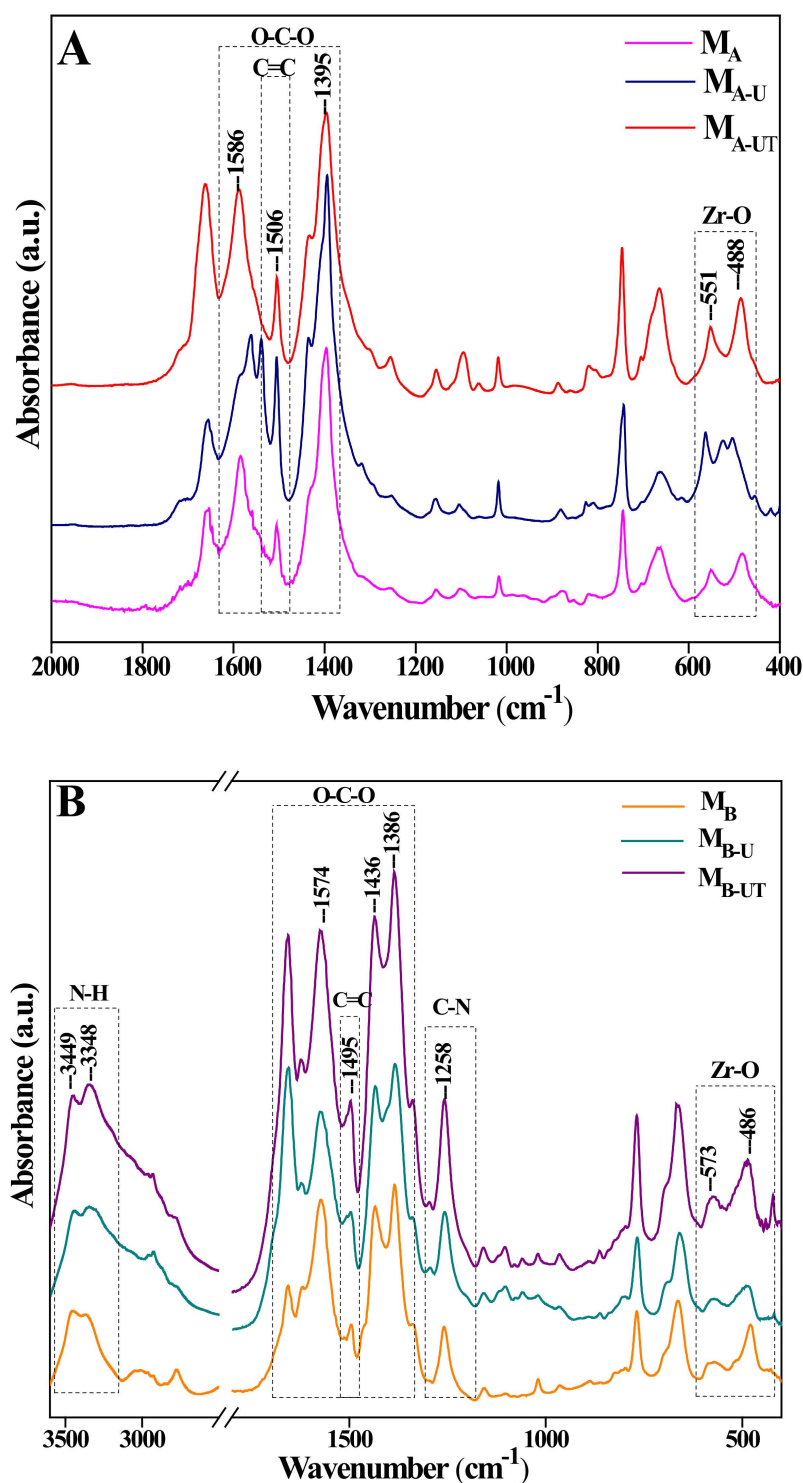


Figure 3. FTIR spectra. (A) UiO-66 magnetic stirring and ultrasound at room temperature and at 60 °C; (B) UiO-66-NH₂ magnetic stirring and ultrasound at room temperature and at 60 °C.

3.1.3. SEM-EDS Analysis

The morphology was characterized by a scanning electron microscope (SEM). Figure 4 shows the synthesized UiO-66 of regular octahedral structure, smooth surface, and good dispersity.

The UiO-66 samples (series A) exhibit a narrow crystal size distribution ranging between 285.7 nm and 488.5 nm, while the UiO-66-NH₂ samples (series B) exhibit smaller particles with a mean crystal size between 209.7 and 406.0 nm (Figure S1).

The Zr, C, O, and N elemental mapping images (Figure S2), show dispersion and homogeneous distribution of these elements on the catalyst surface [44,45].

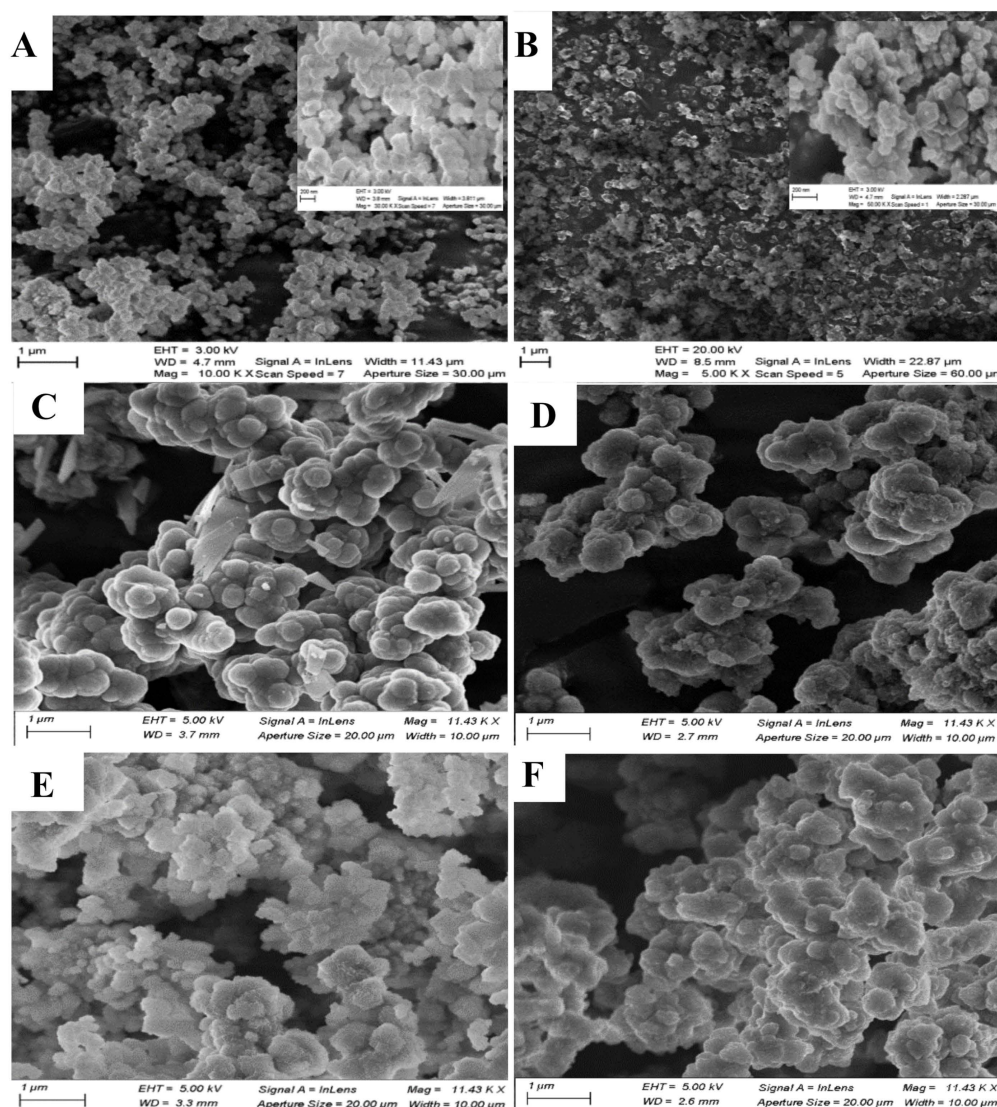


Figure 4. SEM image of (A) M_A , (B) M_B , (C) M_A-U , (D) M_B-U , (E) M_A-UT , and (F) M_B-UT .

3.1.4. Microwave Plasma Atomic Emission Spectrometry (MP-AES) and the Surface Area by BET

Through elemental analysis, the percentage of Zr present in the bulk of the catalyst was determined (Table 1). It is observed that the samples that had a temperature in the synthesis managed to anchor a greater amount of the Zr. Furthermore, comparing the binding agents, those with BDC have a higher % Zr than the others.

To investigate the textural characteristics, N_2 adsorption–desorption isotherms for UiO-66 and UiO-66-NH₂ were measured and these are shown in Figure 5. All materials exhibit type Ib isotherms, where the pore size distributions are in a range including micropores wider than ~ 1 nm and narrow mesopores (of width $< \sim 2.5$ nm) [46]. The N_2 uptake at the low-pressure range ($P/P_0 < 0.3$) suggests the existence of micropores, while the uptake at the middle-pressure range ($P/P_0 > 0.5$) with hysteresis between adsorption and desorption branches is characteristic of mesopores. For the sample M_A , which was synthesized without ultrasonic and temperature treatment, no hysteresis loop was observed on the isotherm, indicating a typical microporous structure. The rest of the samples show H1 type hysteresis loops [46], which at low and high relative pressure belong to

disparate types of isotherms characteristic of solids with microporous windows and partial mesoporous cages [27,47]. Ultrasonic and temperature treatment applied, have decreased the pore size from 2.64 nm to 2.30 nm for series A and from 2.36 nm to 1.07 nm for series B. These comparative results suggest that the ultrasonic and temperature treatments have a significant influence on the pore structures, promoting the presence of a narrow mesopore and micropore distribution. Pore size and surface area in the series B samples have been largely reduced compared with that of series A. This might be because of the introduction of amino groups ($-NH_2$) in the BDC- NH_2 blocking the pores [48]. The surface area reported by the literature indicates higher values than reported in this work, along with lower pore volume values. Wang et al. [49], Su et al. [50], and Hu et al. [48], were reported a surface area of $1110 \text{ m}^2 \text{ g}^{-1}$, $967 \text{ m}^2 \text{ g}^{-1}$, and $1525 \text{ m}^2 \text{ g}^{-1}$, respectively, while the pore volume reported was $0.60 \text{ cm}^3 \text{ g}^{-1}$, $0.57 \text{ cm}^3 \text{ g}^{-1}$, and $0.66 \text{ cm}^3 \text{ g}^{-1}$ corresponding to micropore size distribution. The lower values of pore volume reported in the literature could be attributed to the different time and temperature autoclave steps, as well as the different ways and times stirring was applied in this work.

Table 1. Composition and surface analysis.

Catalyst	Zr (w %) Experimental	BET ($\text{m}^2 \text{ g}^{-1}$)	Pore Size (nm)	Pore Volume ($\text{cm}^3 \text{ g}^{-1}$)
M_A	28.4 ± 0.6	683	2.64	0.248
M_{A-U}	16.5 ± 0.3	640	2.46	0.163
M_{A-UT}	17.2 ± 0.3	658	2.30	0.153
M_B	20.5 ± 0.4	400	2.36	0.164
M_{B-U}	14.8 ± 0.3	300	1.21	0.099
M_{B-UT}	16.2 ± 0.3	312	1.07	0.095

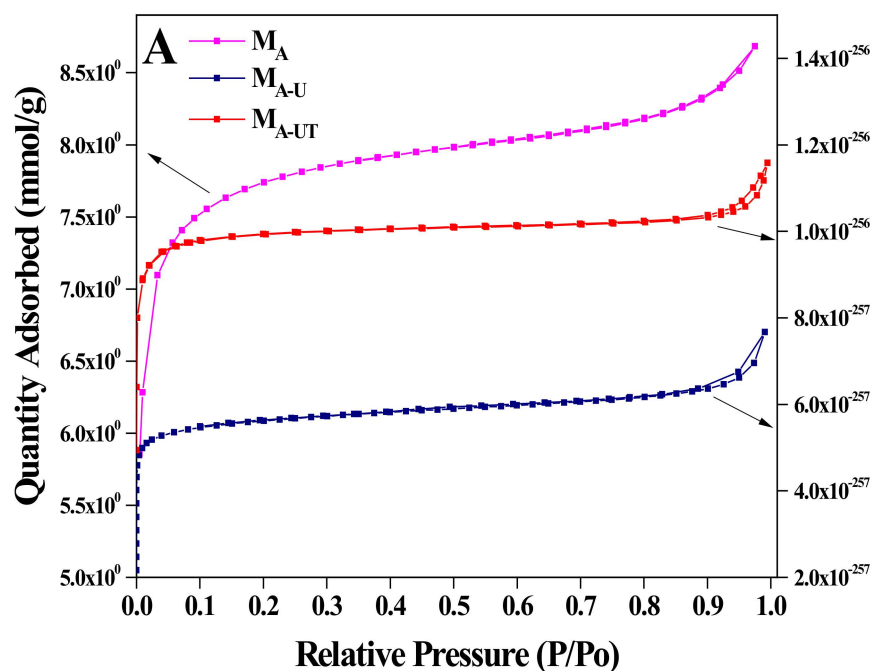


Figure 5. Cont.

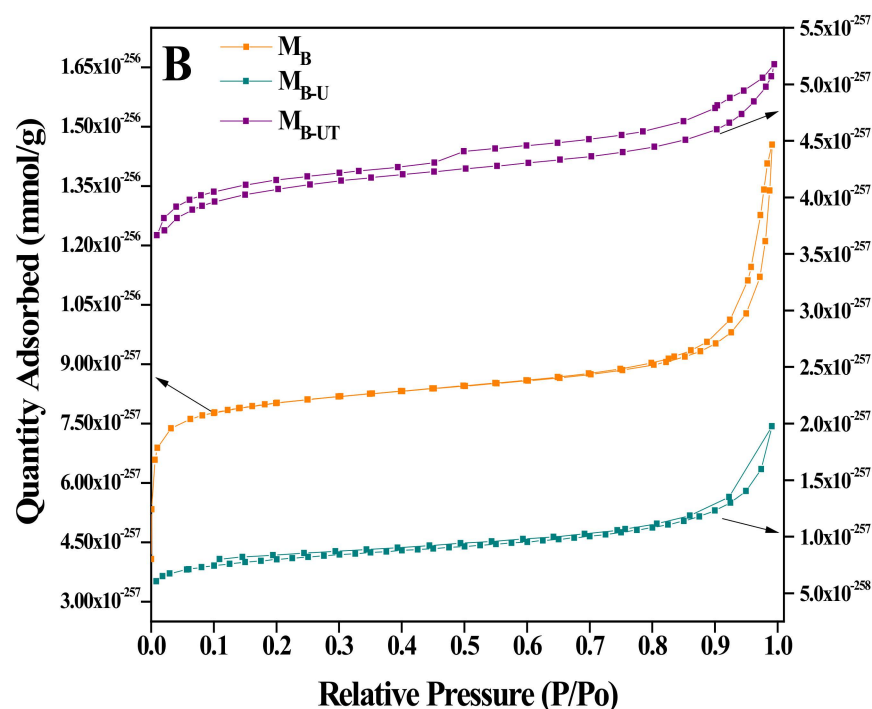


Figure 5. N₂ adsorption–desorption isotherms (A) UiO-66 magnetic stirring and ultrasound at room temperature and at 60 °C; (B) UiO-66-NH₂ magnetic stirring and ultrasound at room temperature and at 60 °C.

3.1.5. XPS-Spectroscopy

The surface composition of the studied catalysts was studied by XPS. Table 2 shows this composition in atomic concentration %. As expected, all samples exhibit a relatively high concentration of C, typical of MOFs materials. The % of C slightly decreases upon using ultrasound and after thermal treatment. Samples of series A show a small % of N due to the use of DMF in the synthesis, without being part of the structure. The % of Zr increases upon using ultrasound. In the case of the catalysts of series B, as expected, the % of N increases due to the presence of the amino group. This percentage increases when using ultrasound.

Table 2. Surface chemical composition (in atomic concentration %) of the studied catalysts determined by XPS.

Sample	C%	Zr%	O%	N%
M _A	62.59	5.59	31.51	0.31
M _A -U	57.94	7.02	34.72	0.33
M _A -UT	56.03	7.76	35.29	0.92
M _B	60.54	4.97	29.87	4.62
M _B -U	57.95	5.63	31.60	4.83
M _B -UT	59.52	5.42	29.96	5.09

The XPS spectra are shown in the Supplementary Material (Figure S3), and in Table 3, the binding energy values in eV for the C 1s, Zr 3d_{5/2}, O 1s, and N 1s signals are included. The catalysts of series A show C 1s core-level spectra composed of two contributions at 284.8 and 288.8 eV. The former and more intense is assigned to –C–C– and –C=C– bonds of adventitious carbon and mainly to the aromatic ring, and the latter to the presence of carboxylic groups. The Zr 3d_{5/2} maxima appear at about 182.8 eV, typical of Zr(IV). The O 1s core-level spectra can be decomposed into two contributions at about 530.1 eV and

531.8 eV. The latter and more intense is assigned to carboxylic oxygen, and the former to lattice oxygen bonded to Zr. The observed higher relative intensity of the contribution at 531.8 eV for samples synthesized with ultrasound is concomitant with the increase in the %Zr (see Table 2). The catalysts of series B show N 1s binding energy values typical of amino groups. The C 1s core-level spectra of these catalysts with amino functional groups show a new contribution at 286.0 eV due to C-N bonds [51].

Table 3. Binding energy values (in eV) of different elements for the studied catalysts. Area percentages are indicated in parentheses.

Sample	C 1s	Zr 3d _{5/2}	O 1s	N 1s
M _A	284.8 (86)	182.8	530.4 (14)	400.6
	288.8 (14)		531.8 (86)	
M _A -U	284.8 (82)	182.8	530.1 (18)	401.4
	288.8 (18)		531.8 (82)	
M _A -UT	284.8 (83)	182.7	530.2 (23)	400.7
	288.8 (17)		531.8 (77)	
M _B	284.8 (64)	182.9	530.3 (12)	399.8
	286.1 (18)		532.0 (88)	
	288.7 (18)			
M _B -U	284.8 (65)	182.9	530.5 (12)	399.5
	286.1 (17)		531.9 (88)	
	288.8 (18)			
M _B -UT	284.8 (65)	182.8	530.6 (17)	399.4
	286.0 (17)		531.9 (83)	
	288.8 (18)			

3.1.6. Acid Analysis by FTIR-CO

The acid sites were studied by FTIR CO adsorbed at different temperatures (50 and 100 °C). The Lewis and Brønsted acid sites were measured by the relative area percentage (Table 4). The sites measured at 50 °C are defined as weak, while those measured at 100 °C are defined as medium [52,53]. The graphs are attached in the Supplementary Material (Figure S4). Making an analysis of the acid sites present, it can be observed that when using ultrasound in the synthesis, an increase in the amount of Lewis acid sites is produced, which could be related to the better catalytic results obtained with said materials. As the acid–base duality is also needed, those with BDC-NH₂ are the ones that produce the best conversion [54].

Table 4. FTIR of CO absorbed.

Sample	% Area (50 °C) Weak Sites		% Area (100 °C) Medium Sites		% Area Total Sites		L/B
	Lewis	Brønsted	Lewis	Brønsted	Lewis	Brønsted	
M _A	45.87	54.13	53.40	46.60	49.64	50.36	0.99
M _A -U	57.38	42.62	52.68	47.32	55.03	44.97	1.22
M _A -UT	60.43	39.57	54.87	45.13	57.65	42.35	1.36
M _B	42.97	57.03	42.74	57.26	42.85	57.15	0.75
M _B -U	45.40	54.60	46.74	53.26	46.07	53.93	0.85
M _B -UT	48.25	51.75	45.75	54.25	47.00	53.00	0.89

3.2. Catalytic Activity: Esterification for Methyl Levulinate Production

Esterification products were identified by gas chromatography with FID and mass spectrometry. The main esterification product was methyl levulinate (ML) and the byproduct was β -lactone from the dehydration of levulinic acid [55–59]. A control experiment was carried out in the absence of catalyst, which gave a negligible methyl levulinate yield of only 1.56%, attributed to the auto-catalysis reaction due to the acidity of levulinic acid [60].

The M_B -UT presented the best yield to the ML (Table 5). These esterification reactions with the presence of the amino group, occur through a dual activation mechanism, related to an acid–base site, in which the Zr sites (acid site) interact with the adsorbed LA while the amino group (basic site), near the Zr, forms an adduct linked to hydrogen in the alcohol molecule, which increases the nucleophilic character of the O atom, favoring the first reaction step [30,33–35]. Due to this behavior, series A without the basic sites ($-NH_2$), showed a lower yield than series B.

Table 5. Catalytic activity. T = 65 °C, 0.05 g catalyst.

Catalyst	Conversion %	Selectivity ML %	Yield %
M_A	16.73	13.41	2.24
M_A -U	42.03	58.31	24.51
M_A -UT	53.85	78.02	42.02
M_B	21.08	73.10	15.41
M_B -U	58.48	84.88	49.64
M_B -UT	63.57	92.22	58.62

By XPS, M_B -U showed a higher Zr (5.63%) content indicating Lewis acid sites, while M_B -UT contains a higher content of N (5.09%) by $-NH_2$ groups, which would indicate more number of basic sites. Better catalytic results are shown in M_B -UT, probably due to the excess of Lewis acid sites as shown in the relation L/B in Table 4 and related with the Zr at the surface as shown in the XPS result. That would ensure that each basic site ($-NH_2$) is close to a Zr, generating a synergistic effect by acid–base duality in the catalyst.

To improve the catalytic performance, some reaction parameters were modified. Prior to it, the catalyst was washed with acetone using ultrasound, centrifuged, and dried at 90 °C, to take out the solvent present in the pores. This allowed the conversion and yield rate to be increased to 70.87% and 67.77%, respectively.

3.2.1. Effect of Reaction Parameters on the LA Esterification with Methanol Catalyzed by M_B -UT

In order to determine the optimal conditions in the catalytic activity of M_B -UT for esterification from LA to ML under reflux conditions, the roles of temperature and reaction time, catalyst loading, and molar ratio of LA to methanol were studied.

Effect of Catalyst Loading

The catalyst mass was varied based on 0.05 g. The catalytic reaction was tested with half, double, and triple of said mass (Table 6). As the catalyst mass increases, the conversion also increases, but this slight increase is not economically justified. Once all the active surface area of the catalyst is occupied by the reactants, the addition of a greater quantity of mass blocks part of its active sites. For this reason, a catalyst mass of 0.05 g was taken as the optimal value.

Table 6. Catalytic activity.

Catalyst Mass	Conversion %	Yield %	$\Delta Y/\Delta C$
0.025 g	56.79	45.22	—
0.05 g	63.57	58.62	536
0.1 g	67.55	63.31	93.8
0.15 g	70.00	65.72	48.2

Effect of Temperature

The original reaction was performed at a temperature close to the boiling point of methanol, so that it does not evaporate while it occurs. Then, the reaction temperature was modified to 55 °C, 60 °C, and 70 °C (Table 7). Although the reaction at 70 °C has the highest conversion, the temperature increase of 5 °C was not justified to increase only 3% of conversion; therefore, the optimal working temperature is 65 °C, a temperature with which a good conversion to the desired product is ensured and also the evaporation of one of the reagents is avoided, which could change the molar ratio between them.

Table 7. Catalytic activity.

Temperature	Conversion %	Selectivity ML %	Yield %	$\Delta Y/\Delta T$
55 °C	48.20	70.29	33.88	----
60 °C	62.86	88.79	55.81	4.26
65 °C	70.87	89.99	63.77	1.59
70 °C	73.79	91.23	67.32	0.71

Effect of Molar Ratio

Regarding the molar ratio of the reagents, we initially worked with a 1:15 ratio of LA: methanol. Variations were performed at a more concentrated point (1:10) and a more dilute point (1:20) (Table 8). In this case, the optimal value corresponds to a ratio of 1:15.

Table 8. Catalytic activity.

Molar Ratio	Conversion %	Yield %	$\Delta Y/\Delta mol [M]$
1:10	59.97	54.19	---
1:15	70.87	63.77	1.92
1:20	67.28	64.47	0.14

3.2.2. Kinetic Model and Estimation of Kinetic Parameters

The esterification reaction of levulinic acid (LA) in the presence of methanol (M) to produce methyl levulinate (ML) and water (W) is given in the reaction below:



The adjustment was made with the experimental data obtained in the batch reaction catalyzed by the M_{B-UT} material. To determine the reaction kinetics, an irreversible reaction and a pseudo-homogeneous model were considered [25,61–63]. Since the alcohol (methanol) is in excess, a zero-order reaction was assumed for it. According to this, the reaction rate is expressed in Equation (5), where [LA] and [M] are the concentrations of levulinic acid and methanol, respectively, [LA₀] is the initial concentration of levulinic acid, k is the rate constant for the forward reactions.

$$-\frac{dC_A}{dt} = k[LA][M] \quad (4)$$

where $[M] \gg [A]$ so $[M] = \text{ctes}$

$$-\frac{dC_A}{dt} = k[LA] \rightarrow -kt = \ln \left[\frac{LA_0}{LA_0 - x} \right] \rightarrow -kt = \ln \frac{[LA_0] \text{ (inicial)}}{[LA_t] \text{ (final)}} \quad (5)$$

$$\ln[LA] = -kt + \ln[LA_0] \rightarrow y = mx + b \text{ (equation of a line)} \quad (6)$$

Furthermore, with the variation of the reaction temperature and by using the Arrhenius Equation (7), it was possible to determine the activation energy and the heat of the reaction [61].

$$k = A e^{-\left(\frac{E_a}{R_g T}\right)} \quad (7)$$

$$\ln(k) = \frac{-E_a}{R_g} \cdot \frac{1}{T} + \ln(A) \rightarrow y = mx + b \text{ (equation of a line)} \quad (8)$$

where E_a , A , and R_g are the activation energy (J/mol), constant “pre-exponential or frequency factor” and ideal gas constant (8.3143 J/mol K), respectively. Both the frequency factor A and the activation energy E_a , are obtained by non-linear regression. The plot of $\ln k$ vs. $1/T$ is plotted by a straight line (Figure S6), the activation energy (E_a) is the slope of the line, and the pre-exponential factor (A) is the ordinate at the origin.

The experimental data were fitted, with pseudo-first-order kinetics, through Equation (6). With the adjustment, a constant kinetic value was obtained $k = 3.57 \times 10^{-3} \text{ min}^{-1}$ with an R^2 of 0.98. As for the activation energy (E_a), adjusted with Equation (8), it yielded a value of 48.99 kJ/mol with an R^2 of 0.98. Additional data have been included as electronic Supplementary Material (Tables S1 and S2, Figures S5 and S6).

3.3. Esterification of Levulinic Acid to Methyl Levulinate in Pressure System, Study of the Stability

For the pressure system, the values obtained are shown in Table 9. It is observed that the conversion and yield results at 1 h of reaction were better for all materials, compared to the batch system at 5 h. The presence of pressure and high temperature in the autoclave system promotes the diffusion of the substrates through the pores of the material and their coordination with the active acid–basic sites, favoring the catalytic performance [41,64–67].

Table 9. Catalytic activity. $T = 130 \text{ }^\circ\text{C}$, $P = 30 \text{ bars}$, 0.05 g catalyst .

Catalyst	Conversion %	Selectivity ML %	Yield %
M_A	50.18	58.63	29.42
M_{A-U}	50.08	67.64	33.87
M_{A-UT}	72.05	87.82	63.27
M_B	73.06	83.11	60.73
M_{B-U}	77.85	100	77.85
M_{B-UT}	85.89 (4) *	100	85.89
$M_{B-UT R1}$	70.18 (24) *	100	70.18
$M_{B-UT R2}$	50.46 (5) *	100	50.46
$M_{B-UT R3}$	40.20 (12) *	63.12	25.37
Cl_4Zr	98.24	100	98.24

* Zr content (ppm) in the supernatant, determined by MP-AES.

To study the stability of the catalyst, three recycles of the reaction were carried out with sample M_{B-UT} ($M_{B-UT R1}$, $M_{B-UT R2}$, $M_{B-UT R3}$); in each recycle, the catalyst was separated from the reaction mixture and dried at $90 \text{ }^\circ\text{C}$. It was observed that the yield decreases while the selectivity is maintained in the first two recycles and falls in the third (Table 9).

By MP-AES, the concentration of Zr in the recycles supernatant was measured, finding values between 5 ppm and 24 ppm, that values represent $\sim(0.5\text{--}2.9)\%$ Zr p/p leached from the solid in each recycle. The activity of the reaction in a homogeneous phase in the presence of Cl_4Zr was also measured, obtaining 98.24% yield to ML. This indicates that the presence of Zr leached in the supernatant did not generate a homogeneous phase reaction or increase the conversion in the recycles as shown in Table 9.

The decrease in catalytic activity can be mainly attributed to the partial blocking of Zr^{+4} sites by electrostatic attraction with ML molecules which cannot be removed by methanol in successive recycles. To support this explanation, after the third recycle catalyst, two reactions with ethanol ($\text{M}_\text{B}\text{-UT R4}$, $\text{M}_\text{B}\text{-UT R5}$) were carried out, obtaining an increase in the conversion (58.66–76.03%) with 100% selectivity (Figure 6).

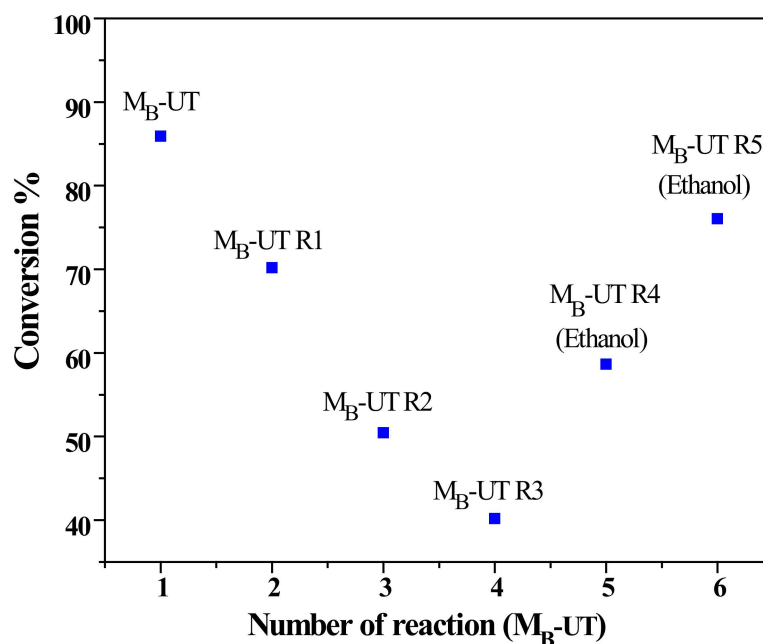


Figure 6. Catalytic activity of the $\text{M}_\text{B}\text{-UT}$ reused with methanol ($\text{M}_\text{B}\text{-UT R1}$, $\text{M}_\text{B}\text{-UT R2}$, $\text{M}_\text{B}\text{-UT R3}$) and ethanol ($\text{M}_\text{B}\text{-UT R4}$, $\text{M}_\text{B}\text{-UT R5}$).

This behavior is attributed to the removal of methyl levulinate molecules on the surface catalyst due to the greater affinity and solubility of ethanol molecules, releasing the Zr^{+4} acid sites.

On the other hand, the $\text{M}_\text{B}\text{-UT R3}$ catalyst was washed with ethanol and ultrasonic stirring, then dried at 90°C and analyzed by FTIR. Figure 7 shows FTIR spectra of $\text{M}_\text{B}\text{-UT}$, $\text{M}_\text{B}\text{-UT}$ used, $\text{M}_\text{B}\text{-UT R3}$, $\text{M}_\text{B}\text{-UT R3}$ supernatant, and $\text{M}_\text{B}\text{-UT R3}$ washed.

The characteristic peaks associated at COO^- , $\text{C}=\text{C}$, $\text{Zr}-\text{O}$, $\text{Zr}(\text{OC})$ groups were maintained in $\text{M}_\text{B}\text{-UT}$ used and $\text{M}_\text{B}\text{-UT R3}$ catalyst.

A peak at $\sim 1716\text{ cm}^{-1}$ associated with ML in the supernatant $\text{M}_\text{B}\text{-UT R3}$, is correlated with the peak in the $\text{M}_\text{B}\text{-UT}$ used and $\text{M}_\text{B}\text{-UT R3}$ indicating the ML adsorbed on the catalyst after use. A decrease in the intensity of this peak after $\text{M}_\text{B}\text{-UT R3}$ washed with ethanol indicates the removal of ML molecules coordinated with acid sites Zr^{+4} on the surface.

XRD patterns of the catalysts ($\text{M}_\text{B}\text{-UT}$, $\text{M}_\text{B}\text{-UT}$ used, and $\text{M}_\text{B}\text{-UT R3}$) are shown in Figure S7. The intensity and the crystalline order of the MOFs phase were maintained after each recycle and mainly after the third one.

Finally, a decrease in catalytic activity with the successive reuse of the catalyst could be mainly related to the blockade of Zr^{+4} acid sites by ML and to a lesser extent by the leachate of this metal.

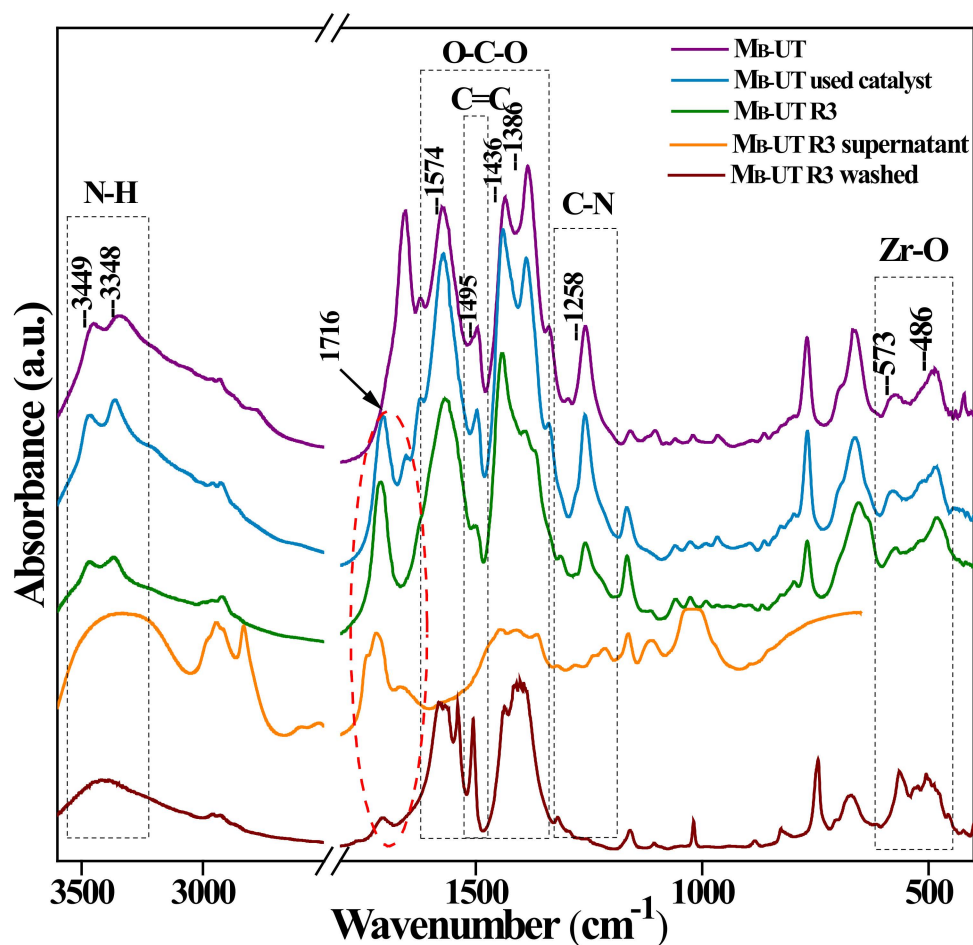


Figure 7. FTIR spectra for the fresh, used catalysts and supernatant reaction.

4. Conclusions

The synthesized materials presented outstanding crystallinity and porosity properties. The implementation of ultrasound and temperature in the synthesis promoted the formation of a micro/mesoporous structure, with crystal sizes between ~ 209.7 and ~ 488.5 nm and a homogeneous distribution of Zr, C, O, and N on the surface, which can be corroborated by BET and SEM analyses. Regarding the catalytic evaluation in a batch system, the materials of each series synthesized with ultrasound at 60°C exhibited the highest conversions, where the M_B -UT sample is the one that presented the best activity, with a yield of 67.77% for the methyl levulinate. The optimal working conditions for this were 65°C , 0.05 g of the catalyst and a mol ratio of reactants of 1:15 (LA:M). These results are associated with the greater dispersion of Lewis acid sites available to catalyze the reaction and also with the acid–base duality due to the $-\text{NH}_2$ group. This dual mechanism involves LA interacting with Zr (Lewis acid site) while the alcohol forms a hydrogen bond with the amino group (basic site). This simultaneous acid–base interaction favors the first reaction step.

A pseudo-homogeneous model was adjusted to first-order kinetics with a value of the reaction constant $k = 3.57 \times 10^{-3} \text{ min}^{-1}$ and activation energy of 48.99 kJ/mol, with an R^2 of 0.98 for both parameters.

Improvements in the catalytic results were achieved, using more severe conditions, through the use of pressure reactors with greater selectivity to the desired product and reduction in the reaction time from 5 to 1 h. The deactivated catalyst observed in the successive recycles is mainly related to the blocking of the Zr^{+4} acid sites by electrostatic attraction of the ML molecules and, to a lesser extent, to the leaching of this metal. The spent material can be activated by ethanol washing allowing the catalytic activity to be maintained in the recycles.

Finally, it can be said that the synthesis of levulinate compounds from levulinic acid derived from biomass using heterogeneous catalysts such as UiO-66 and UiO-66-NH₂ is a highly viable and efficient alternative, which allows eco-compatible reactions to be carried out with the medium, with easy separation of the products of interest.

Supplementary Materials: The following supporting information can be downloaded at: <https://www.mdpi.com/article/10.3390/chemengineering6020026/s1>, Additional information about the XPS graphics, the particle size, the EDS images, the XRD pattern for the used catalyst, the CO-FTIR absorption spectra, the kinetics of the reaction, and the adjustments made have been included in the file supplied as Supplementary Materials.

Author Contributions: Conceptualization, A.C.H. and M.E.C.; methodology, D.A.B.F.; validation, A.C.H., M.E.C. and D.A.B.F.; formal analysis, E.R.-C., S.M.M., A.C.H., M.E.C. and D.A.B.F.; investigation, E.R.-C., S.M.M., A.C.H., M.E.C. and D.A.B.F.; writing—original draft preparation, D.A.B.F.; writing—review and editing, A.C.H., M.E.C. and E.R.-C.; supervision, M.E.C. and E.R.-C. All authors have read and agreed to the published version of the manuscript.

Funding: Projects PID-UTN-SCyT (MATCBCO 008094TC and MAIAICO 6570TC) Universidad Tecnológica Nacional. Projects RTI2018-099668-BC22 of Ministerio de Ciencia, Innovación y Universidades, and UMA18-FEDERJA- 126 and P20_00375 of Junta de Andalucía and FEDER funds.

Data Availability Statement: Not applicable.

Acknowledgments: Financial support from the Consejo Nacional de Investigaciones Científicas y Tecnológicas (CONICET) and Universidad Tecnológica Nacional–Facultad Regional Córdoba (UTN-FRC). E.R.C. thanks to project RTI2018-099668-BC22 of Ministerio de Ciencia, Innovación y Universidades, and projects UMA18-FEDERJA-126 and P20_00375 of Junta de Andalucía and FEDER funds.

Conflicts of Interest: The authors declare no conflict of interest.

References

1. Han, X.; Guo, Y.; Liu, X.; Xia, Q.; Wang, Y. Catalytic conversion of lignocellulosic biomass into hydrocarbons: A mini review. *Catal. Today* **2019**, *319*, 2–13. [CrossRef]
2. Climent, M.J.; Corma, A.; Iborra, S. Conversion of biomass platform molecules into fuel additives and liquid hydrocarbon fuels. *Green Chem.* **2014**, *16*, 516–547. [CrossRef]
3. Romanelli, G.P.; Ruiz, D.M.; Pasquale, G.A. *Química de la Biomasa y los Biocombustibles*; Editorial de la Universidad Nacional de La Plata (EDULP): Buenos Aires, Argentina, 2020. [CrossRef]
4. Adeleye, A.T.; Louis, H.; Akakuru, O.U.; Joseph, I.; Enudi, O.C.; Michael, D.P. A Review on the conversion of levulinic acid and its esters to various useful chemicals. *AIMS Energy* **2019**, *7*, 165–185. [CrossRef]
5. Corma Canos, A.; Iborra, S.; Velty, A. Chemical routes for the transformation of biomass into chemicals. *Chem. Rev.* **2007**, *107*, 2411–2502. [CrossRef]
6. Yu, Z.; Lu, X.; Xiong, J.; Ji, N. Transformation of levulinic acid to valeric biofuels: A review on heterogeneous bifunctional catalytic systems. *ChemSusChem* **2019**, *12*, 3915–3930. [CrossRef]
7. Serrano-Ruiz, J.C.; Pineda, A.; Balu, A.M.; Luque, R.; Campelo, J.M.; Romero, A.A.; Ramos-Fernández, J.M. Catalytic transformations of biomass-derived acids into advanced biofuels. *Catal. Today* **2012**, *195*, 162–168. [CrossRef]
8. Dutta, S.; Bhat, N.S. Recent advances in the value addition of biomass-derived levulinic acid: A review focusing on its chemical reactivity patterns. *ChemCatChem* **2021**, *13*, 3202–3222. [CrossRef]
9. Omoruyi, U.; Page, S.; Hallett, J.; Miller, P.W. Homogeneous catalyzed reactions of levulinic acid: To γ -valerolactone and beyond. *ChemSusChem* **2016**, *9*, 2037–2047. [CrossRef]
10. Jeong, H.; Park, S.Y.; Ryu, G.H.; Choi, J.H.; Kim, J.H.; Choi, W.S.; Lee, S.M.; Choi, J.W.; Choi, I.G. Catalytic conversion of hemicellulosic sugars derived from biomass to levulinic acid. *Catal. Commun.* **2018**, *117*, 19–25. [CrossRef]
11. Badgujar, K.C.; Bhanage, B.M. Thermo-chemical energy assessment for production of energy-rich fuel additive compounds by using levulinic acid and immobilized lipase. *Fuel Process. Technol.* **2015**, *138*, 139–146. [CrossRef]
12. Bhat, N.S.; Mal, S.S.; Dutta, S. Recent advances in the preparation of levulinic esters from biomass-derived furanic and levulinic chemical platforms using heteropoly acid (HPA) catalysts. *Mol. Catal.* **2021**, *505*, 111484. [CrossRef]
13. Ogino, I.; Suzuki, Y.; Mukai, S.R. Esterification of levulinic acid with ethanol catalyzed by sulfonated carbon catalysts: Promotional effects of additional functional groups. *Catal. Today* **2018**, *314*, 62–69. [CrossRef]
14. Démolis, A.; Essayem, N.; Rataboul, F. Synthesis and applications of alkyl levulinates. *ACS Sustain. Chem. Eng.* **2014**, *2*, 1338–1352. [CrossRef]

15. Bart, H.J.; Reidetschläger, J.; Schatka, K.; Lehmann, A. Kinetics of esterification of succinic anhydride with methanol by homogeneous catalysis. *Int. J. Chem. Kinet.* **1994**, *26*, 1013–1021. [[CrossRef](#)]
16. Gong, W.; Liu, Y.; Li, H.; Cui, Y. Metal-organic frameworks as solid Brønsted acid catalysts for advanced organic transformations. *Coord. Chem. Rev.* **2020**, *420*, 213400. [[CrossRef](#)]
17. Qu, H.; Liu, B.; Gao, G.; Ma, Y.; Zhou, Y.; Zhou, H.; Li, L.; Li, Y.; Liu, S. Metal-organic framework containing Brønsted acidity and Lewis acidity for efficient conversion glucose to levulinic acid. *Fuel Process. Technol.* **2019**, *193*, 1–6. [[CrossRef](#)]
18. Sun, Y.; Zhou, H.C. Recent progress in the synthesis of metal-organic frameworks. *Sci. Technol. Adv. Mater.* **2015**, *16*, 54202. [[CrossRef](#)]
19. Czaja, A.U.; Trukhan, N.; Müller, U. Industrial applications of metal-organic frameworks. *Chem. Soc. Rev.* **2009**, *38*, 1284–1293. [[CrossRef](#)]
20. Stock, N.; Biswas, S. Synthesis of metal-organic frameworks (MOFs): Routes to various MOF topologies, morphologies, and composites. *Chem. Rev.* **2012**, *112*, 933–969. [[CrossRef](#)]
21. Lillerud, K.P.; Cavka, J.H.; Lamberti, C.; Guillou, N.; Bordiga, S.; Jakobsen, S.; Olsbye, U. A new zirconium inorganic building brick forming metal organic frameworks with exceptional stability. *J. Am. Chem. Soc.* **2008**, *130*, 13850–13851. [[CrossRef](#)]
22. Rahmawati, I.D.; Ediati, R.; Prasetyoko, D. Synthesis of UiO-66 using solvothermal method at high temperature. *IPTEK J. Proc. Ser.* **2014**, *1*, 42–46. [[CrossRef](#)]
23. Abid, H.R.; Shang, J.; Ang, H.M.; Wang, S. Amino-functionalized Zr-MOF nanoparticles for adsorption of CO₂ and CH₄. *Int. J. Smart Nano Mater.* **2013**, *4*, 72–82. [[CrossRef](#)]
24. Bai, Y.; Dou, Y.; Xie, L.H.; Rutledge, W.; Li, J.R.; Zhou, H.C. Zr-based metal-organic frameworks: Design, synthesis, structure, and applications. *Chem. Soc. Rev.* **2016**, *45*, 2327–2367. [[CrossRef](#)] [[PubMed](#)]
25. Cirujano, F.G.; Corma, A.; Llabrés i Xamena, F.X. Zirconium-containing metal organic frameworks as solid acid catalysts for the esterification of free fatty acids: Synthesis of biodiesel and other compounds of interest. *Catal. Today* **2015**, *257*, 213–220. [[CrossRef](#)]
26. Wei, R.; Gaggioli, C.A.; Li, G.; Islamoglu, T.; Zhang, Z.; Yu, P.; Farha, O.K.; Cramer, C.J.; Gagliardi, L.; Yang, D.; et al. Tuning the properties of Zr₆O₈ nodes in the metal organic framework UiO-66 by selection of node-bound ligands and linkers. *Chem. Mater.* **2019**, *31*, 1655–1663. [[CrossRef](#)]
27. Li, H.; Chu, H.; Ma, X.; Wang, G.; Liu, F.; Guo, M.; Lu, W.; Zhou, S.; Yu, M. Efficient heterogeneous acid synthesis and stability enhancement of UiO-66 impregnated with ammonium sulfate for biodiesel production. *Chem. Eng. J.* **2021**, *408*, 127277. [[CrossRef](#)]
28. Herbst, A.; Janiak, C. MOF catalysts in biomass upgrading towards value-added fine chemicals. *CrystEngComm* **2017**, *19*, 4092–4117. [[CrossRef](#)]
29. Caratelli, C.; Hajek, J.; Cirujano, F.G.; Waroquier, M.; Llabrés i Xamena, F.X.; Van Speybroeck, V. Nature of active sites on UiO-66 and beneficial influence of water in the catalysis of Fischer esterification. *J. Catal.* **2017**, *352*, 401–414. [[CrossRef](#)]
30. Cirujano, F.G.; Corma, A.; Llabrés i Xamena, F.X. Conversion of levulinic acid into chemicals: Synthesis of biomass derived levulinate esters over Zr-containing MOFs. *Chem. Eng. Sci.* **2015**, *124*, 52–60. [[CrossRef](#)]
31. Garibay, S.J.; Cohen, S.M. Isoreticular synthesis and modification of frameworks with the UiO-66 topology. *Chem. Commun.* **2010**, *46*, 7700–7702. [[CrossRef](#)]
32. Lozano, L.A.; Iglesias, C.M.; Faroldi, B.M.C.; Ulla, M.A.; Zamaro, J.M. Efficient solvothermal synthesis of highly porous UiO-66 nanocrystals in dimethylformamide-free media. *J. Mater. Sci.* **2018**, *53*, 1862–1873. [[CrossRef](#)]
33. Ramli, N.A.S.; Zaharudin, N.H.; Amin, N.A.S. Esterification of renewable levulinic acid to levulinate esters using amberlyst-15 as a solid acid catalyst. *J. Teknol.* **2017**, *79*, 137–142. [[CrossRef](#)]
34. Liang, X.; Fu, Y.; Chang, J. Sustainable production of methyl levulinate from biomass in ionic liquid-methanol system with biomass-based catalyst. *Fuel* **2020**, *259*, 116246. [[CrossRef](#)]
35. Di, X.; Zhang, Y.; Fu, J.; Yu, Q.; Wang, Z.; Yuan, Z. Biocatalytic upgrading of levulinic acid to methyl levulinate in green solvents. *Process Biochem.* **2019**, *81*, 33–38. [[CrossRef](#)]
36. Chaffey, D.R.; Bere, T.; Davies, T.E.; Apperley, D.C.; Taylor, S.H.; Graham, A.E. Conversion of levulinic acid to levulinate ester biofuels by heterogeneous catalysts in the presence of acetals and ketals. *Appl. Catal. B Environ.* **2021**, *293*, 120219. [[CrossRef](#)]
37. Rubio-Martinez, M.; Batten, M.P.; Polyzos, A.; Carey, K.C.; Mardel, J.I.; Lim, K.S.; Hill, M.R. Versatile, high quality and scalable continuous flow production of metal-organic frameworks. *Sci. Rep.* **2014**, *4*, 5443. [[CrossRef](#)]
38. Lu, A.X.; McEntee, M.; Browe, M.A.; Hall, M.G.; Decoste, J.B.; Peterson, G.W. MOFabric: Electrospun nanofiber mats from PVDF/UiO-66-NH₂ for chemical protection and decontamination. *ACS Appl. Mater. Interfaces* **2017**, *9*, 13632–13636. [[CrossRef](#)]
39. Kandiah, M.; Nilsen, M.H.; Usseglio, S.; Jakobsen, S.; Olsbye, U.; Tilsted, M.; Larabi, C.; Quadrelli, E.A.; Bonino, F.; Lillerud, K.P. Synthesis and stability of tagged UiO-66 Zr-MOFs. *Chem. Mater.* **2010**, *22*, 6632–6640. [[CrossRef](#)]
40. Ragon, F.; Horcajada, P.; Chevreau, H.; Hwang, Y.K.; Lee, U.H.; Miller, S.R.; Devic, T.; Chang, J.S.; Serre, C. In situ energy-dispersive X-ray diffraction for the synthesis optimization and scale-up of the porous zirconium terephthalate UiO-66. *Inorg. Chem.* **2014**, *53*, 2491–2500. [[CrossRef](#)]
41. Arrozi, U.S.F.; Wijaya, H.W.; Patah, A.; Permana, Y. Efficient acetalization of benzaldehydes using UiO-66 and UiO-67: Substrates accessibility or Lewis acidity of zirconium. *Appl. Catal. A Gen.* **2015**, *506*, 77–84. [[CrossRef](#)]
42. Luu, C.L.; Van Nguyen, T.T.; Nguyen, T.; Hoang, T.C. Synthesis, characterization and adsorption ability of UiO-66-NH₂. *Adv. Nat. Sci. Nanosci. Nanotechnol.* **2015**, *6*, 025004. [[CrossRef](#)]

43. Ding, Y.; Wei, F.; Dong, C.; Li, J.; Zhang, C.; Han, X. UiO-66 based electrochemical sensor for simultaneous detection of Cd(II) and Pb(II). *Inorg. Chem. Commun.* **2021**, *131*, 108785. [[CrossRef](#)]
44. Han, Y.; Liu, M.; Li, K.; Zuo, Y.; Wei, Y.; Xu, S.; Zhang, G.; Song, C.; Zhang, Z.; Guo, X. Facile synthesis of morphology and size-controlled zirconium metal-organic framework UiO-66: The role of hydrofluoric acid in crystallization. *CrystEngComm* **2015**, *17*, 6434–6440. [[CrossRef](#)]
45. Hou, J.; Luan, Y.; Tang, J.; Wensley, A.M.; Yang, M.; Lu, Y. Synthesis of UiO-66-NH₂ derived heterogeneous copper (II) catalyst and study of its application in the selective aerobic oxidation of alcohols. *J. Mol. Catal. A Chem.* **2015**, *407*, 53–59. [[CrossRef](#)]
46. Thommes, M.; Kaneko, K.; Neimark, A.V.; Olivier, J.P.; Rodriguez-Reinoso, F.; Rouquerol, J.; Sing, K.S.W. Physisorption of gases, with special reference to the evaluation of surface area and pore size distribution (IUPAC Technical Report). *Pure Appl. Chem.* **2015**, *87*, 1051–1069. [[CrossRef](#)]
47. Ye, C.; Qi, Z.; Cai, D.; Qiu, T. Design and synthesis of ionic liquid supported hierarchically porous zirconium metal-organic framework as a novel Brønsted-Lewis acidic catalyst in biodiesel synthesis. *Ind. Eng. Chem. Res.* **2019**, *58*, 1123–1132. [[CrossRef](#)]
48. Hu, Z.; Peng, Y.; Kang, Z.; Qian, Y.; Zhao, D. A modulated hydrothermal (MHT) approach for the facile synthesis of UiO-66-type MOFs. *Inorg. Chem.* **2015**, *10*, 4862–4868. [[CrossRef](#)] [[PubMed](#)]
49. Wang, F.; Chen, Z.; Chen, H.; Goetjen, T.A.; Li, P.; Wang, F.X.; Alayoglu, S.; Ma, K.; Chen, Y.; Wang, T.; et al. Interplay of Lewis and Brønsted acid sites in Zr-based metal-organic frameworks for efficient esterification of biomass-derived levulinic acid. *ACS Appl. Mater. Interfaces* **2019**, *11*, 32090–32096. [[CrossRef](#)] [[PubMed](#)]
50. Su, Y.; Zhang, Z.; Liu, H.; Wang, Y. Cd_{0.2}Zn_{0.8}S@UiO-66-NH₂ nanocomposites as efficient and stable visible-light-driven photocatalyst for H₂ evolution and CO₂ reduction. *Appl. Catal. B Environ.* **2017**, *200*, 448–457. [[CrossRef](#)]
51. Moulder, J.F.; Stickle, W.F.; Sobol, P.E.; Bomben, K.D. *Handbook of X-ray Photoelectron Spectroscopy*; Perkin-Elmer Corp., Eden Prairie: Chichester, UK, 1992; ISBN 9780470014226.
52. Wiersum, A.D.; Soubeyrand-Lenoir, E.; Yang, Q.; Moulin, B.; Guillermin, V.; Yahia, M.B.; Burrelly, S.; Vimont, A.; Miller, S.; Vagner, C.; et al. An evaluation of UiO-66 for gas-based applications. *Chem.-Asian J.* **2011**, *6*, 3270–3280. [[CrossRef](#)]
53. Timofeeva, M.N.; Panchenko, V.N.; Jun, J.W.; Hasan, Z.; Matrosova, M.M.; Jhung, S.H. Effects of linker substitution on catalytic properties of porous zirconium terephthalate UiO-66 in acetalization of benzaldehyde with methanol. *Appl. Catal. A Gen.* **2014**, *471*, 91–97. [[CrossRef](#)]
54. Strauss, I.; Chakarova, K.; Mundstock, A.; Mihaylov, M.; Hadjiivanov, K.; Guschanski, N.; Caro, J. UiO-66 and UiO-66-NH₂ based sensors: Dielectric and FTIR investigations on the effect of CO₂ adsorption. *Microporous Mesoporous Mater.* **2020**, *302*, 110227. [[CrossRef](#)]
55. Caretto, A.; Perosa, A. Upgrading of levulinic acid with dimethylcarbonate as solvent/reagent. *ACS Sustain. Chem. Eng.* **2013**, *1*, 989–994. [[CrossRef](#)]
56. Langlois, D.P.; Wolff, H. Pseudo esters of levulinic acid. *J. Am. Chem. Soc.* **1948**, *70*, 2624–2626. [[CrossRef](#)]
57. Lima, C.G.S.; Monteiro, J.L.; de Melo Lima, T.; Weber Paixão, M.; Corrêa, A.G. Angelica lactones: From biomass-derived platform chemicals to value-added products. *ChemSusChem* **2018**, *11*, 25–47. [[CrossRef](#)]
58. Al-Shaal, M.G.; Ciptonugroho, W.; Holzhäuser, F.J.; Mensah, J.B.; Hausoul, P.J.C.; Palkovits, R. Catalytic upgrading of α -angelica lactone to levulinic acid esters under mild conditions over heterogeneous catalysts. *Catal. Sci. Technol.* **2015**, *5*, 5168–5173. [[CrossRef](#)]
59. Ramli, N.A.S.; Sivasubramaniam, D.; Amin, N.A.S. Esterification of levulinic acid using ZrO₂-supported phosphotungstic acid catalyst for ethyl levulinate production. *Bioenergy Res.* **2017**, *10*, 1105–1116. [[CrossRef](#)]
60. Nandiwale, K.Y.; Sonar, S.K.; Niphadkar, P.S.; Joshi, P.N.; Deshpande, S.S.; Patil, V.S.; Bokade, V.V. Catalytic upgrading of renewable levulinic acid to ethyl levulinate biodiesel using dodecatungstophosphoric acid supported on desilicated H-ZSM-5 as catalyst. *Appl. Catal. A Gen.* **2013**, *460–461*, 90–98, ISBN 9120259026. [[CrossRef](#)]
61. Zubir, M.I.; Chin, S.Y. Kinetics of modified Zirconia-catalyzed heterogeneous esterification reaction for biodiesel production. *J. Appl. Sci.* **2010**, *10*, 2584–2589. [[CrossRef](#)]
62. Jrad, A.; Abu Tarboush, B.J.; Hmadeh, M.; Ahmad, M. Tuning acidity in zirconium-based metal organic frameworks catalysts for enhanced production of butyl butyrate. *Appl. Catal. A Gen.* **2019**, *570*, 31–41. [[CrossRef](#)]
63. Emel'yanenko, V.N.; Altuntepe, E.; Held, C.; Pimerzin, A.A.; Verevkin, S.P. Renewable platform chemicals: Thermochemical study of levulinic acid esters. *Thermochim. Acta* **2018**, *659*, 213–221. [[CrossRef](#)]
64. Feng, J.; Li, M.; Zhong, Y.; Xu, Y.; Meng, X.; Zhao, Z.; Feng, C. Hydrogenation of levulinic acid to γ -valerolactone over Pd@UiO-66-NH₂ with high metal dispersion and excellent reusability. *Microporous Mesoporous Mater.* **2020**, *294*, 109858. [[CrossRef](#)]
65. Cao, W.; Lin, L.; Qi, H.; He, Q.; Wu, Z.; Wang, A.; Luo, W.; Zhang, T. In-situ synthesis of single-atom Ir by utilizing metal-organic frameworks: An acid-resistant catalyst for hydrogenation of levulinic acid to Γ -valerolactone. *J. Catal.* **2019**, *373*, 161–172. [[CrossRef](#)]
66. Sosa, L.F.; da Silva, V.T.; de Souza, P.M. Hydrogenation of levulinic acid to γ -valerolactone using carbon nanotubes supported nickel catalysts. *Catal. Today* **2020**, *381*, 86–95. [[CrossRef](#)]
67. Tulchinsky, M.L.; Briggs, J.R. One-pot synthesis of alkyl 4-alkoxy-pentanoates by esterification and reductive etherification of levulinic acid in alcoholic solutions. *ACS Sustain. Chem. Eng.* **2016**, *4*, 4089–4093. [[CrossRef](#)]